

Suppression of moving-potential effect in an optical Raman lattice scheme for spin-orbit-coupled alkaline-earth fermions

Rui Wu(吴瑞), Han Zhang(张涵), Tao Deng(邓涛), Wen-Wei Wang(王文伟), and Xibo Zhang(张熙博)
Citation: Chin. Phys. B, 2026, 35 (**6**): 067102. DOI: 10.1088/1674-1056/ae4c71
http://cpb.iphy.ac.cn; http://iopscience.iop.org/cpb

What follows is a list of articles you may be interested in

Thickness dependence of linearly polarized light-induced momentum anisotropy and inverse spin Hall effect in topological insulator Bi_2Te_3

Jiayi Qiu(邱嘉毅), Jinling Yu(俞金玲), Zhu Diao(刁佇), Yunfeng Lai(赖云锋), Shuying Cheng(程树英), Yonghai Chen(陈涌海), and Ke He(何珂)
Chin. Phys. B, 2025, 34 (**11**): 117103. DOI: 10.1088/1674-1056/adf82a

Effect of lattice distortion on spin admixture and quantum transport in organic devices with spin-orbit coupling

Ying Wang(王莹), Dan Li(李丹), Xinying Sun(孙新英), Huiqing Zhang(张惠晴), Han Ma(马晗), Huixin Li(李慧欣), Junfeng Ren(任俊峰), Chuankui Wang(王传奎), and Guichao Hu(胡贵超)
Chin. Phys. B, 2024, 33 (**7**): 077101. DOI: 10.1088/1674-1056/ad35ae

Investigation of helicity-dependent photocurrent of surface states in $(Bi_{0.7}Sb_{0.3})_2Te_3$ nanoplate

Qin Yu(喻钦), Jinling Yu(俞金玲), Yonghai Chen(陈涌海), Yunfeng Lai(赖云锋), Shuying Cheng(程树英), and Ke He(何珂)
Chin. Phys. B, 2024, 33 (**5**): 057101. DOI: 10.1088/1674-1056/ad322c

Highly anisotropic Dirac fermion and spin transportproperties in Cu-graphane

Chao Wu(吴超), Lichuan Zhang(张礼川), Lin Xia(夏霖), Dong Hao(郝东), Shiqi Li(李仕琪), Lizhi Zhang(张礼智), Yuee Xie(谢月娥), and Yuanping Chen(陈元平)
Chin. Phys. B, 2023, 32 (**8**): 087104. DOI: 10.1088/1674-1056/accff1

Rashba spin-orbit coupling induced rectified currents in monolayer graphene with exchange field and sublattice potential

Liang Chen(陈亮), Feng Li(李峰), and Xiao-Ming Ding(丁晓明)
Chin. Phys. B, 2023, 32 (**8**): 087103. DOI: 10.1088/1674-1056/acc932

RAPID COMMUNICATION

Suppression of moving-potential effect in an optical Raman lattice scheme for spin–orbit-coupled alkaline-earth fermions

Rui Wu(吴瑞)[1,2,3,†], Han Zhang(张涵)[1,2,3,†], Tao Deng(邓涛)[1,2,3,4], Wen-Wei Wang(王文伟)[1,2,3], and Xibo Zhang(张熙博)[1,2,3,4,‡]

[1] *International Center for Quantum Materials, School of Physics, Peking University, Beijing* 100871, *China*
[2] *Collaborative Innovation Center of Quantum Matter, Beijing* 100871, *China*
[3] *Hefei National Laboratory, Hefei* 230088, *China*
[4] *Beijing Academy of Quantum Information Sciences, Beijing* 100193, *China*

(Received 29 January 2026; revised manuscript received 24 February 2026; accepted manuscript online 3 March 2026)

Optical Raman lattices in ultra-cold alkali-metal and alkaline-earth atoms provide a powerful method to synthesize spin–orbit (SO) coupling. While the ground-state energy splittings (divided by Planck's constant) can reach the range of tens of megahertz in alkali-metal atoms, the typical ground-state energy splittings are on the order of tens of kilohertz or smaller in alkaline-earth atoms (AEAs) such as ^{87}Sr. For AEAs, because such limited ground-state energy splittings are rather close to the kilohertz-scale recoil energy that is relevant for optical lattice physics, a standard implementation of a two-dimensional (2D) optical Raman lattice can lead to parasitic periodic moving potentials that heat up the atoms and severely limit the atomic lifetime. Recently, an improved optical Raman lattice scheme was proposed and experimentally realized in ultra-cold strontium fermions, which significantly enhanced the lifetime of 2D-SO-coupled fermions. However, a concrete electro-optical setup has yet to be demonstrated, and its control precision needs to be quantified. Here we demonstrate the electro-optical setup of an improved optical Raman lattice scheme that suppresses the effect of moving lattice potentials for alkaline-earth fermions by introducing a sufficiently large frequency separation between two sets of laser polarization components, where each set yields an independent Raman coupling. To quantify the precision of this setup, we feedback-control the relative phase between the two sets of Raman couplings, which is an important parameter characterizing the 1D–2D crossover of SO couplings, and measure the stability of this phase over hour-long periods. We also investigate the optimum range for the applied frequency separation. Our approach provides a useful tool that helps achieve long-lived SO-coupled systems using AEAs.

Keywords: spin–orbit coupling, optical Raman lattice, alkaline-earth atoms, ultracold fermions, moving potential

PACS: 71.70.Ej, 37.10.Jk, 67.85.Lm

DOI: 10.1088/1674-1056/ae4c71 **CSTR:** 32038.14.CPB.ae4c71

1. Introduction

Since the realization of spin–orbit (SO) coupling in ultracold atoms,[1–4] much progress has been made in emulating two- and higher-dimensional SO couplings,[5–11] opening paths for exploring non-Abelian gauge potentials[12,13] and exotic topological physics such as topological superfluid phases.[14,15] Due to the magnetic insensitivity of their ground states, alkaline-earth atoms (AEAs) have emerged as a promising platform for realizing a rich variety of SO-coupled few-level systems, including a 3D SO-coupled nodal-line semimetal,[16] the Qi–Wu–Zhang model for quantum anomalous Hall physics,[17] as well as a spin-momentum lattice.[18] However, in these works,[16–18] the lifetime of SO-coupled AEAs is on the level of 10 ms, signaling some underlying mechanism for heating up the atoms associated with the substantially smaller two-level energy splitting in SO-coupled AEAs than in alkali-metal atoms.

In a recent work that realized SO-coupled topological fermions beyond the rotating wave approximation (RWA),[19] the lifetime of the system was successfully enhanced by an order of magnitude to the 100-ms level. There are two key ingredients of the improved experimental setup. The first is the implementation of a highly isolated few-level system using a highly nonlinear spin-discriminating method based on optical a.c. Stark shifts.[20] The second is the suppression of moving lattice potentials associated with the relatively small ground-state level splitting in AEAs, as schematically illustrated in Fig. 1. This issue arises because the frequency difference δf between the Raman beams needs to be tuned to be close to the relatively small ground-state level splitting δf_0 for exploring near-resonant SO physics. In a standard optical Raman lattice configuration[8,17] (referred to as the "single-tone" scheme) shown in Figs. 1(c) and 1(d), two laser beams ("Raman 1" and "Raman 2") intersect at the atoms with a relatively

[†] These authors contributed equally to this work.
[‡] Corresponding author. E-mail: xibo@pku.edu.cn
© 2026 Chinese Physical Society and IOP Publishing Ltd. All rights, including for text and data mining, AI training, and similar technologies, are reserved.

small frequency difference δf (tens of kilohertz or smaller for AEAs under the single-tone scheme), where the combination of the vertical polarization component of one beam and the horizontal polarization component of the other beam gives rise to a set of two-photon Raman transitions. However, the optical interference due to other combinations, such as the two vertical polarization components, can lead to moving lattice potentials with a speed of $v = \pi|\delta f/k_{\rm mov}|$, where $k_{\rm mov}$ is the component of the wavevector along the direction of the moving potential. Unless the characteristic speed v is sufficiently large that the atoms cannot follow the moving potential, which is the case for SO-coupled alkali-metal atoms,[7,8] atoms will in general experience heating due to the moving lattice potentials. In Ref. [19], the heating rate for SO-coupled strontium (Sr) Fermi gases due to moving lattice potentials has been reduced by a factor of 500 based on increasing v to a sufficiently large value, which is very beneficial for enhancing the atomic lifetime. However, a concrete electro-optical setup and the precision of the method have yet to be demonstrated for their further applications in other SO-coupled AEA systems.

In this article, we report on the electro-optical setup and performance of the improved optical Raman lattice scheme (referred to as the dual-tone scheme), which has been successfully applied in Ref. [19] but has not yet been described in detail. This scheme is implemented using two-spin strontium (^{87}Sr) Fermi gases with 2D SO couplings induced by optical Raman lattices. While the two Raman lasers are far-detuned from the $^1{\rm S}_0 \rightarrow {}^3{\rm P}_1$ single-photon intercombination transitions with narrow, kilohertz-level linewidths, two-photon Raman transitions can be induced between a pair of spin ground states. In the dual-tone scheme, a sufficiently large frequency separation is introduced between two groups of polarization components of the Raman beams. While each group gives rise to an independent two-photon Raman coupling, two polarization components from different groups have distinct frequencies, and the corresponding interference effect is suppressed, which flattens the moving lattice potential over characteristic time scales for AEAs in optical lattices. Furthermore, the relative phase between these two sets of Raman couplings is measured and controlled to an instability below 10^{-4} radians. Finally, the optimum regime for the frequency separation is studied based on simultaneously minimizing the perturbation to a cold Fermi gas and keeping the lattice imperfection within an acceptable level. The dual-tone scheme significantly improves the stability of 2D-SO-coupled AEAs and holds promise for promoting the exploration of long-lived SO-coupled systems and interaction-induced correlation physics.

2. The dual-tone optical Raman lattice scheme

This improved scheme introduces a tunable, large frequency separation between pairs of polarization components that can lead to spin-conserving moving lattice potentials without altering the relatively small two-photon detuning for the spin-flipping Raman couplings for ^{87}Sr Fermi gases. Here, the scheme utilizes a pair of adjacent spin ground states separated by $\delta f_0 \approx 50$ kHz: $|\uparrow\rangle \equiv {}^1{\rm S}_0|F = \frac{9}{2}, m_F = -\frac{9}{2}\rangle$ and $|\downarrow\rangle \equiv |\frac{9}{2}, -\frac{7}{2}\rangle$, where the quantization axis is defined by an externally applied magnetic field $\boldsymbol{B}$ along the Z (vertical) direction; see Figs. 1(a) and 1(b). The frequencies of the two Raman lasers are chosen to be close to 689.452 nm, which correspond to detunings of about -0.9 GHz relative to the $^1{\rm S}_0|F = \frac{9}{2}\rangle \rightarrow {}^3{\rm P}_1|F' = \frac{11}{2}\rangle$ single-photon transition under zero magnetic field. Each combination of a spin-conserving π-polarization component and a spin-changing σ-polarization component of the laser electric fields gives rise to an independent two-photon Raman coupling between $|\uparrow\rangle$ and $|\downarrow\rangle$. As shown in Fig. 1(b), a 2D optical Raman lattice is formed by intersecting two laser beams (Raman 1 and Raman 2) that propagate along the X-direction (E_1) and Y-direction (E_2), respectively, intersect at the atoms, and are then phase-shifted and retro-reflected. On one hand, the retro-reflection leads to the interference of the same polarization components with opposite wavevectors, which gives rise to spin-conserving, spatially periodic static potentials (namely, optical lattices) and corresponds to the diagonal elements of the Hamiltonian of the two-spin ^{87}Sr Fermi gases. The depths of optical lattices are determined by both the laser intensities and the atomic polarizabilities that in turn depend on the single-photon laser detunings, laser polarizations, the associated atomic states, and the corresponding Clebsch–Gordan coefficients. On the other hand, each combination of a vertical electric field (providing the π-polarization component) and a horizontal electric field (containing the needed σ-polarization component) leads to an independent set of Raman couplings, which correspond to the spin-flipping off-diagonal elements of the Hamiltonian. The Raman coupling strengths are determined by the electric field amplitudes, the single-photon detunings, the associated atomic states, and the corresponding Clebsch–Gordan coefficients. Because the 0.9-GHz detuning is comparable to the ^{87}Sr $^3{\rm P}_1$ hyperfine splittings, a summation of the contributions from all three excited-state hyperfine manifolds needs to be performed over $F' = \frac{7}{2}$, $\frac{9}{2}$, and $\frac{11}{2}$ in order to obtain an accurate evaluation of experimental parameters.

We refer to the two groups of orthogonal polarization components, (E_{1Y}, E_{2Z}) and (E_{1Z}, E_{2X}) as the "0" manifold and the "Δ" manifold, respectively. Each manifold of polarization components gives rise to a two-photon Raman transition with characteristic coupling strengths of Ω_{01} and Ω_{02}, which are indicated by the purple and green colors in Figs. 1(a) and 1(b). While in each manifold, the two polarization components have the same small frequency difference δf (tuned to be close to the ground-state level splitting δf_0 for exploring near-resonant SO physics), the two manifolds are separated

by a frequency difference Δ, which under large Δ values will significantly suppress the effect of the time-varying a.c. Stark potentials due to the polarization pairs (E_{1Z}, E_{2Z}) and (E_{1Y}, E_{2X}).[19] By contrast, under $\Delta = 0$, the experimental scheme reduces to a "standard" experimental configuration, which we refer to as the single-tone optical Raman lattice scheme (Figs. 1(c) and 1(d)). With $\Delta = 0$, the polarization pairs (E_{1Z}, E_{2Z}) and (E_{1Y}, E_{2X}) give rise to pernicious moving lattice potentials with a speed of $v = \pi|\delta f/k_{\rm mov}|$, which can

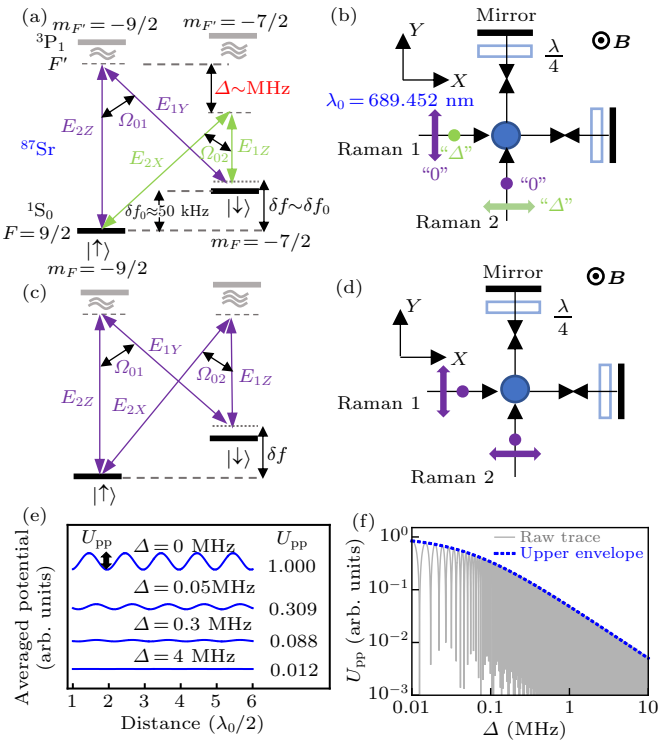


Fig. 1. Schematic of the setups for the dual-tone and standard single-tone optical Raman lattice schemes based on ^{87}Sr fermions. (a) Energy diagram of the dual-tone scheme for implementing the optical Raman lattices, which suppresses the moving-potential effect by introducing a frequency difference Δ between the orthogonal polarizations of the laser along each spatial direction. Here, $|\uparrow\rangle$ and $|\downarrow\rangle$ correspond to a pair of spin ground states, $^1S_0|F=\frac{9}{2}, m_F=-\frac{9}{2}\rangle$ and $|\frac{9}{2},-\frac{7}{2}\rangle$, which are separated by an energy splitting of about $\delta f_0 \approx 50$ kHz. The $^3P_1$ manifold allows for $F'=\frac{7}{2}$, $\frac{9}{2}$, and $\frac{11}{2}$. The polarization components E_{2Z} and E_{1Y} (E_{1Z} and E_{2X}) in the "0" ("Δ") manifold induce Raman coupling Ω_{01} (Ω_{02}), without forming harmful interference between inter-manifold components. (b) Optical setup of the dual-tone scheme. The 2D Raman lattices are formed by two laser beams with wavelengths of about 689.452 nm, corresponding to large, gigahertz-level single-photon red detunings with respect to the $^1S_0 \rightarrow {}^3P_1$ transitions of kilohertz linewidths. These beams propagate along the X direction (E_1) and Y direction (E_2), intersect at the atoms (blue sphere), and are then retro-reflected. The frequency difference δf between the Raman beams is chosen to be close to δf_0 for exploring near-resonant SO physics. The components with purple (green) color correspond to the "0" ("Δ") manifold of E_{2Z} and E_{1Y} (E_{1Z} and E_{2X}). B denotes the magnetic field. (c) Energy diagram of a standard single-tone scheme for implementing optical Raman lattice,[8,17,21] corresponding to a special case of $\Delta = 0$ in (a). (d) Optical setup of the single-tone scheme. (e) The moving lattice potential averaged over $t_0 = h/E_0 \approx 0.21$ ms. Here, h denotes the Planck's constant and the recoil energy E_0 is used as the typical energy scale for 2D optical Raman lattice. The time-averaged potential becomes flatter when Δ increases from near zero to 4 MHz, which is quantified by its peak-to-peak value $U_{\rm pp}$ (normalized by the value at $\Delta = 0$). (f) Variation of $U_{\rm pp}$ as a function of Δ. The oscillatory behavior (gray solid line) arises from the averaging process, where the time-averaged potential vanishes at particular detunings. The blue dashed line indicates an upper envelope with an asymptotic Δ^{-1} behavior.

severely heat up a cold Fermi gas.[17] Figure 1(e) illustrates the moving lattice potential averaged over a characteristic time scale of $h/E_0 \approx 0.21$ ms under several different Δ values, where h is the Planck's constant and E_0 is the recoil energy for the wavelength of $\lambda_0 = 689.452$ nm and ^{87}Sr atoms. For a moving lattice potential due to the interference betweeen E_{1Z} and E_{2Z}, the overall reduction of the moving-potential effect with the increase of Δ is shown by the peak-to-peak modulation depth, $U_{\rm pp}$, of the averaged moving lattice potentials; see Fig. 1(f). The solid gray line represents the exact computation, exhibiting a nodal structure due to the finite averaging time. The blue dashed line indicates an upper envelope with an asymptotic Δ^{-1} behavior. At $\Delta = 4$ MHz, $U_{\rm pp}$ is reduced by two orders of magnitude compared to that in the single-tone scheme. The significantly reduced $U_{\rm pp}$ corresponds to a physical picture that under typical time scales in optical lattices, cold atoms cannot follow the fast-moving lattice potentials and therefore become largely immune to the corresponding heating effect. Here, without loss of generality, we have assumed a typical condition of $\delta f = 50$ kHz based on experimental parameters. In the following sections, we utilize a value of $\Delta = 4$ MHz.

We implement a relatively large frequency difference Δ in the dual-tone scheme based on acousto-optic frequency shifting. Figure 2(a) shows the optical setup, which resembles the form of a Mach–Zehnder interferometer. A laser beam is first split into two paths using a polarizing beam splitter (PBS1). The transmitted beam (purple line) remains at the original frequency, whereas the reflected beam (green line) passes through two acousto-optic modulators (AOM1, AOM2) with opposite frequency shifts that differ by Δ. The two beams are then recombined by a second beam splitter (PBS2), yielding two output beams that correspond to the Raman 1 and Raman 2 beams also shown in Fig. 1. In the Raman 1 and Raman 2 paths, additional modulators AOM3 and AOM4 introduce slightly different frequency shifts with the same sign and a small frequency difference of δf. Each Raman beam goes through a short single-mode polarization-maintaining optical fiber to ensure high spatial-mode quality and stable beam pointing before interacting with the atoms.

3. Phase detection and stabilization

With the increased number of optics in the dual-tone scheme, it is important to precisely control the relative phase between two sets of Raman couplings, which characterizes the 1D–2D crossover of SO physics.[17] Figures 2(b) and 2(c) illustrate the optical and electronic setups for the phase detection and phase stabilization respectively. As shown in Figs. 1(a) and 2(a), the four laser polarization components $E_{1Z,1Y,2Z,2X}$ can be described by

$$E_{1Z} = E_{1Z,0}\, e^{i[k_0 x + 2\pi(\nu_0 - \Delta)t + \alpha]}, \tag{1}$$

$$E_{1Y} = E_{1Y,0}\, e^{i(k_0 x + 2\pi\nu_0 t + \alpha')}, \tag{2}$$

$$E_{2Z} = E_{2Z,0}\, e^{i[k_0 y + 2\pi(\nu_0 + \delta f)t + \beta]}, \tag{3}$$

$$E_{2X} = E_{2X,0}\, e^{i[k_0 y + 2\pi(\nu_0 - \Delta + \delta f)t + \beta']}, \tag{4}$$

where $\nu_0 \approx 434.827$ THz is the laser frequency, $k_0 = 2\pi/\lambda_0$ is the angular wave-number, $E_{1Z/1Y/2Z/2X,0}$ are amplitudes of $E_{1Z,1Y,2Z,2X}$, α and α' (β and β') are the initial phases for the Raman 1 (Raman 2) polarization components. The relative phase $\delta\varphi$ between the two sets of Raman couplings depends on the initial phases and can be written as[8,17,21]

$$\delta\varphi = \alpha - \alpha' + \beta - \beta'. \tag{5}$$

As shown in Fig. 2(b), the phase difference between two polarization components in each Raman beam is determined by directing the sampled beam through a polarizer oriented at an oblique angle and then onto a photo-detector (PD, Thorlabs PDA100A2) to measure an optical beat. Detectors PD1 and PD2 record the intensity oscillations that reveal the phase differences $\alpha' - \alpha$ for Raman 1 and $\beta - \beta'$ for Raman 2, respectively:

$$I_1 = |E_{1Z}|^2 + |E_{1Y}|^2 + 2|E_{1Z}||E_{1Y}|\cos(2\pi\Delta t + \alpha' - \alpha),$$
$$I_2 = |E_{2Z}|^2 + |E_{2X}|^2 + 2|E_{2Z}||E_{2X}|\cos(2\pi\Delta t + \beta - \beta').$$

These phase differences contain the contributions from air flow, thermal drift, polarization-dependent fiber phase fluctuation, and phase shifts induced by reflective and transmissive optical elements.

The aforementioned photo-detector outputs are further processed and utilized for precise feedback control of the relative phase $\delta\varphi$. As shown in Fig. 2(c), we remove the d.c. components of the detector outputs via bias tees (Mini–Circuits ZFBT-4R2GW+), amplify the a.c. components by radio-frequency (RF) amplifiers (Mini–Circuits ZFL-1000+), and then compare their phases using a low-noise RF mixer (Mini–Circuits ZFM-2-S+). After being low-pass filtered, the mixer output signal $V_{\rm m}$ is proportional to a sinusoidal function of $\delta\varphi$:

$$V_{\rm m} \propto \cos(\alpha - \alpha' + \beta - \beta') = \cos(\delta\varphi). \tag{6}$$

This signal serves as the error signal for feedback control and is fed into a servo controller (Nakai technology, PID-001) with a PI corner frequency of 3.2 kHz. Here, we use a high-voltage amplifier (Thorlabs HVA200) to provide the driving d.c. voltage for an electro-optic modulator (Thorlabs EO–PM-NR-C1) that serves as a phase actuator and tunes $\delta\varphi$ by changing the phase difference between two orthogonal polarization components of the Raman 1 beam. Similarly, we generate a second mixed signal (using mixer 2 in Fig. 2(b)) to provide an out-of-loop monitoring signal for $\delta\varphi$.

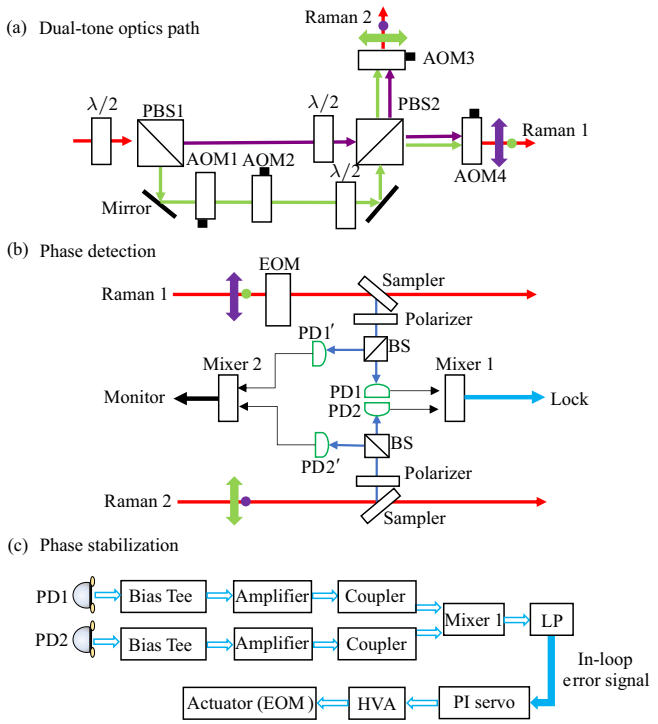


Fig. 2. Electro-optical setups for the dual-tone scheme and the corresponding optical phase control. (a) Optical path for the dual-tone scheme. An incoming laser beam is split into two paths by a polarizing beam splitter (PBS1), frequency-shifted in one path, and recombined at another polarizing beam splitter (PBS2). Two acousto-optic modulators (AOM1 and AOM2) with opposite diffraction orders and distinct driving frequencies generate a frequency difference of Δ between the two paths. The transmitted and reflected output ports of PBS2 prepare the Raman 1 and Raman 2 lasers in Fig. 1, respectively. (b) Phase detection. The PD1 (PD2) photo-detector measures a beat that contains the frequency and phase difference between orthogonal polarization components of the Raman 1 (Raman 2) laser. The PD1 and PD2 beats are then compared by a radio-frequency (RF) mixer, which yields an RF signal whose phase fluctuation corresponds to the fluctuation of the relative phase $\delta\varphi$ between two Raman couplings. The mixer 1 output is used as an in-loop error signal for the feedback control of $\delta\varphi$, while the mixer 2 output serves as an out-of-loop monitoring signal. (c) Phase stabilization. The in-loop error signal is fed into a feedback servo to stabilize $\delta\varphi$, with an electro-optic modulator (EOM) serving as the phase actuator and a high-voltage amplifier (HVA) providing sufficient actuation range. Here, "coupler" denotes directional coupler and "LP" denotes low-pass filter.

4. Results

To characterize the precision of the optical phase control system, we measure the in-loop error signal and out-of-loop monitoring signal for the relative phase $\delta\varphi$ between two Raman couplings. The voltage signal (proportional to $\cos\delta\varphi$) is measured with a data logger (National Instruments cDAQ-SV1101) with a sampling interval of 10 ms, normalized by the maximum voltage, and converted to a phase signal. In Fig. 3(a), the gray dots indicate the free-running $\delta\varphi$, which drifts with a peak-to-peak value of about 0.4π over an hour. Under active feedback control, the phase stability is greatly enhanced, as shown by both the in-loop error (black dots) and out-of-loop monitoring (red dots) signals. We further quantify the precision of the achieved phase control based on an analysis using the Allan deviation (ADEV).[22] Figure 3(b) shows the ADEVs of the in-loop and out-of-loop phase data simi-

lar to those in Fig. 3(a) under active feedback control, where the error bars are estimated based on five one-hour-long data sets. Both the in-loop and out-of-loop signals show excellent stability better than the 10^{-4}-radian level at an averaging time of 0.02–655 s. The achieved control precision of $\delta\varphi$ shows that the dual-tone optical Raman lattice scheme is robust against environmental fluctuations, which thereby significantly improves the stability of SO-coupled systems.

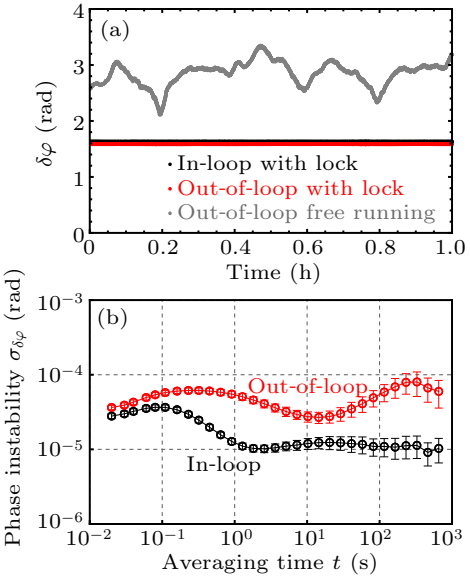


Fig. 3. Precision of the optical phase control system. (a) Time traces of the relative phase between two sets of Raman couplings, recorded over one hour. The gray dots indicate the free-running relative phase, while the black and red dots represent the feedback-controlled relative phase and the corresponding out-of-loop monitoring signal, respectively. (b) The Allan deviation of the relative phase $\delta\varphi$ for the in-loop error signal and out-of-loop monitoring signal under active stabilization, based on multiple data sets similar to (a). The shown data are the result of averaging over five groups of measurements. Error bars represent 1σ statistical uncertainty.

Finally, we demonstrate the choice of optimum regime for the frequency separation Δ based on a compromise between flattening the moving lattice potential and restricting the mismatch between two sets of optical lattices in the dual-tone scheme. On one hand, we characterize the suppression of the heating effect for a cold strontium Fermi gas associated with the moving lattice potentials under various Δ values using the maximum optical depth (OD) in the atomic images. A Fermi gas of ^{87}Sr atoms is slowly loaded into a 2D optical Raman lattice and further held for a period of time, after which a 15-ms time-of-flight measurement is performed. In Fig. 4, we observe that, as Δ increases, the maximum OD quickly increases and saturates after Δ exceeds 0.2 MHz. Here, all atomic images are scaled by one global factor such that the scaled maximum OD reaches about unity at sufficiently large Δ values. On the other hand, as Δ increases, a discrepancy develops between the two sets of static optical lattices formed by polarization components in the "0" manifold and those in the "Δ" manifold, manifesting as a mismatch of their potential minima (normalized by the lattice constant $a_{\mathrm{Lat}} = \lambda_0/2$) near the atoms. As shown by the red dashed line in Fig. 4, the lattice site position mismatch exceeds 0.02 a_{Lat} for $\Delta \geq 6$ MHz, which is less desirable. Therefore, we judge that the range of 0.2–6 MHz is fairly applicable for Δ, and that our experimental choice of $\Delta \approx 4$ MHz is near-optimal.

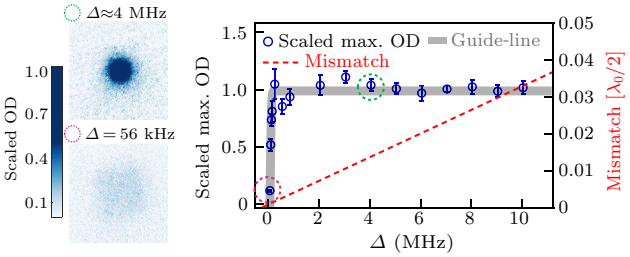


Fig. 4. Determination of the appropriate range for the frequency separation between two laser frequency manifolds. A spin-polarized Fermi gas is slowly loaded into the 2D optical Raman lattice under different frequency separations Δ from 56 kHz to about 10 MHz. The maximum optical depth (OD) of 2D-SO-coupled atoms (blue circle) is recorded after a 15-ms time-of-flight (TOF) process to provide a quantitative figure of merit for optimizing Δ. Here, all atomic images are scaled by one global factor such that the scaled maximum OD reaches about unity at sufficiently large Δ values. At small Δ values, moving lattice potentials heat up atoms and reduce the atomic OD. On the other hand, large Δ values lead to substantial mismatch between two sets of lattices due to the "0" and "Δ" manifolds (red dashed line), which is computed assuming a typical distance of 50 cm between atoms and the retro-reflecting mirrors. The left two insets are the atomic clouds corresponding to $\Delta \approx 4$ MHz and $\Delta = 56$ kHz, respectively. Error bars represent 1σ statistical uncertainty.

5. Discussion and conclusion

In summary, we have depicted a detailed dual-tone scheme for implementing optical Raman lattices and SO couplings in AEAs with significantly suppressed moving-potential effect. The optimum regime for the frequency separation parameter Δ has been demonstrated. The method described in this work holds promise for realizing SO-coupled topological systems with long lifetimes[19] using a variety of alkaline-earth fermions and for future exploration of interaction-induced correlation physics[23–27].

Acknowledgements

We thank Zhi-Ang Chen, Shize Du, Hao-Ran Zeng and Run-Qi Lei for insightful discussions and technical support. This work was supported by the Chinese Academy of Sciences Strategic Priority Research Program (Grant No. XDB35020100), the Hefei National Laboratory, and the Innovation Program for Quantum Science and Technology (Grant No. 2021ZD0301903).

References

[1] Zhai H 2015 *Rep. Prog. Phys.* **78** 026001
[2] Zhang L and Liu X J 2018 *Synthetic spin–orbit coupling in cold atoms*, Ed. Zhang W, Yi W and Sá de Melo C A R (Singapore: World Scientific) p. 1
[3] Dalibard J, Gerbier F, Juzeliūnas G and Öhberg P 2011 *Rev. Mod. Phys.* **83** 1523
[4] Galitski V and Spielman I B 2013 *Nature* **494** 49

[5] Huang L, Meng Z, Wang P, Peng P, Zhang S L, Chen L, Li D, Zhou Q and Zhang J 2016 *Nat. Phys.* **12** 540

[6] Meng Z, Huang L, Peng P, Li D, Chen L, Xu Y, Zhang C, Wang P and Zhang J 2016 *Phys. Rev. Lett.* **117** 235304

[7] Wu Z, Zhang L, Sun W, Xu X T, Wang B Z, Ji S C, Deng Y, Chen S, Liu X J and Pan J W 2016 *Science* **354** 83

[8] Sun W, Wang B Z, Xu X T, Yi C R, Zhang L, Wu Z, Deng Y, Liu X J, Chen S and Pan J W 2018 *Phys. Rev. Lett.* **121** 150401

[9] Xu X T, Wang Z Y, Jiao R H, Yi C R, Sun W and Chen S 2019 *Rev. Sci. Instrum.* **90** 054708

[10] Wang Z Y, Cheng X C, Wang B Z, Zhang J Y, Lu Y H, Yi C R, Niu S, Deng Y, Liu X J, Chen S and Pan J W 2021 *Science* **372** 271

[11] Zhang J Y, Yi C R, Zhang L, Jiao R H, Shi K Y, Yuan H, Zhang W, Liu X J, Chen S and Pan J W 2023 *Phys. Rev. Lett.* **130** 043201

[12] Osterloh K, Baig M, Santos L, Zoller P and Lewenstein M 2005 *Phys. Rev. Lett.* **95** 010403

[13] Ruseckas J, Juzeliūnas G, Öhberg P and Fleischhauer M 2005 *Phys. Rev. Lett.* **95** 010404

[14] Qu C, Zheng Z, Gong M, Xu Y, Mao L, Zou X, Guo G and Zhang C 2013 *Nat. Commun.* **4** 2710

[15] Liu X J, Law K T and Ng T K 2014 *Phys. Rev. Lett.* **112** 086401

[16] Song B, He C, Niu S, Zhang L, Ren Z, Liu X J and Jo G B 2019 *Nat. Phys.* **15** 911

[17] Liang M C, Wei Y D, Zhang L, Wang X J, Zhang H, Wang W W, Qi W, Liu X J and Zhang X 2023 *Phys. Rev. Res.* **5** L012006

[18] Lauria P, Kuo W T, Cooper N R and Barreiro J T 2022 *Phys. Rev. Lett.* **128** 245301

[19] Zhang H, Wang W W, Qiao C, Zhang L, Liang M C, Wu R, Wang X J, Liu X J and Zhang X 2024 *Sci. Bull.* **69** 747

[20] Wang W W, Zhang H, Qiao C, Liang M C, Wu R and Zhang X 2023 *Front. Phys.* **18** 62303

[21] Wang B Z, Lu Y H, Sun W, Chen S, Deng Y and Liu X J 2018 *Phys. Rev. A* **97** 011605

[22] Riley W J 2008 *Handbook of Frequency Stability Analysis* (*NIST Special Publication* vol. 1065) (National Institute of Standards and Technology)

[23] Zhang C, Tewari S, Lutchyn R M and Das Sarma S 2008 *Phys. Rev. Lett.* **101** 160401

[24] Sato M, Takahashi Y and Fujimoto S 2009 *Phys. Rev. Lett.* **103** 020401

[25] Zhu S L, Shao L B, Wang Z D and Duan L M 2011 *Phys. Rev. Lett.* **106** 100404

[26] Pan J S, Liu X J, Zhang W, Yi W and Guo G C 2015 *Phys. Rev. Lett.* **115** 045303

[27] Poon T F J and Liu X J 2018 *Phys. Rev. B* **97** 020501